ARTICLES
PUBLISHED ONLINE: 19 SEPTEMBER 2010 | DOI: 10.1038/NMAT2858
nature materials

Unusual infrared-absorption mechanism in thermally reduced graphene oxide

M. Acik[1], G. Lee[1], C. Mattevi[2†], M. Chhowalla[2†], K. Cho[1] and Y. J. Chabal[1*]

Infrared absorption of atomic and molecular vibrations in solids can be affected by electronic contributions through non-adiabatic interactions, such as the Fano effect. Typically, the infrared-absorption lineshapes are modified, or infrared-forbidden modes are detectable as a modulation of the electronic absorption. In contrast to such known phenomena, we report here the observation of a giant-infrared-absorption band in reduced graphene oxide, arising from the coupling of electronic states to the asymmetric stretch mode of a yet-unreported structure, consisting of oxygen atoms aggregated at the edges of defects. Free electrons are induced by the displacement of the oxygen atoms, leading to a strong infrared absorption that is in phase with the phonon mode. This new phenomenon is only possible when all other oxygen-containing chemical species, including hydroxyl, carboxyl, epoxide and ketonic functional groups, are removed from the region adjacent to the edges, that is, clean graphene patches are present.

Graphene, with its sp^2-hybridized honeycomb two-dimensional carbon lattice consisting of conjugated hexagonal cells[1], shows extraordinary properties because of its dimensionality and unique electronic band structure[2]. Graphene is a semimetallic carbon material with linear dispersion[3] because its carriers behave as Dirac fermions (zero effective mass)[4], which suppresses carrier backscattering[5]. Consequently, interesting physical properties have been demonstrated, such as high intrinsic carrier mobility (between 3,000 and ~200,000 $cm^2 V^{-1}s^{-1}$; ref. 6), room-temperature ballistic transport on a submicrometre scale[7] with large mean free path[8], enhanced Coulomb interaction[9], suppression of weak localization[10] and deviation from the adiabatic Born–Oppenheimer approximation[11].

The use of graphene for actual devices depends on the ability to fabricate finite-size structures and control edge formation with chemical stability. To this end, much needs to be learned about the chemistry and the physical properties of various forms of graphene-based materials. Graphene oxidation (or even hydration) is known for instance to remove states at the Fermi level, thus producing an insulator. It is therefore expected that oxygen attachment to graphene in any chemical form (epoxide, hydroxyl, carboxyl and ketonic-type functional groups) both on the basal plane[12] and at the edges[13] reduces electronic states at the Fermi level, that is, conductivity, as shown experimentally[14]. Graphene oxide is indeed a good insulator that only partially recovers a weak conductivity on reduction. Even after high-temperature annealing (800–1,100 °C), there is some remaining oxygen (~8–10 at.%) in partially reduced single-layer graphene oxide (GO-1L), which contains nearly 20% of sp^3-hybridized carbon[15]. It is therefore unlikely that partially reduced GO exhibits any measurable property involving free electrons.

We report here the observation of a surprisingly strong infrared absorption band that occurs only on reduction of graphene oxide. This band is assigned to a specific mode (asymmetric C–O–C stretch) of a previously unreported oxide structure, involving oxygen located in the basal plane (forming C–O–C bonds) at the edges of defective areas in reduced graphene oxide (that is, clean graphene areas). This very specific edge configuration (cyclic edge ether) results in part from short-range mass transport during reduction (conversion of oxygen species to edge ethers) and constitutes the most stable form of oxygen in graphene. The large enhancement in infrared absorption is attributed to the resonant induction by edge-oxygen motion of mobile electrons localized in the vicinity of the oxygen. These free electrons provide another (dominant) absorption channel. The generation of free electrons is specific to only one normal mode associated with this particular edge configuration, namely the asymmetric stretch of the C–O–C moiety. All other modes present a normal infrared absorption.

This giant absorption is a new phenomenon specific to graphene-based structures, distinct from non-adiabatic phenomena at surfaces[16]. It suggests a means of developing sensitive bandpass filters[17], resonant detectors[18], thermal-infrared remote sensors[19] (night vision), antennas[20] and solar absorbers for energy harvesting[21], and of fabricating high-performance devices[22].

To appreciate the special oxygen configuration found after high-temperature annealing, it is necessary to characterize a uniformly deposited GO-1L thin film using a vacuum filtration method[15,23] before and after thermal annealing. Figure 1 shows a representative infrared-absorbance spectrum of an initial GO-1L, that is, obtained before any thermal reduction, with contributions from hydroxyl (C–OH), ketonic species (C=O), carboxyl (COOH), sp^2-hybridized C=C (in-plane vibrations), epoxide (C–O–C) and various C–O and C=O containing chemical species such as lactol, peroxide, dioxolane, anhydride and cyclic ether, which fall in the three spectral regions labelled α, β and γ characteristic of ether-like and ketone-like species.

The evolution of the infrared differential spectra due to gradual removal of oxygen-containing species on thermal reduction in vacuum is investigated by measuring the evolution of infrared-absorption spectra (Supplementary Fig. S1, Section S1). Almost all the oxygen-containing species disappear after annealing to 750 °C (Supplementary Fig. S1d), with only a very small concentration (~5–7 at.%) of C–O containing ether groups in GO-1L, as shown by very weak features in the 700–1,320 cm^{-1} range. Intensity changes

[1]Department of Materials Science and Engineering, University of Texas at Dallas, Richardson, Texas 75080, USA, [2]Rutgers University, Materials Science and Engineering, Piscataway, New Jersey 08854, USA. †Present address: Department of Materials, Imperial College, London, SW7 2AZ, UK.
*e-mail: chabal@utdallas.edu.

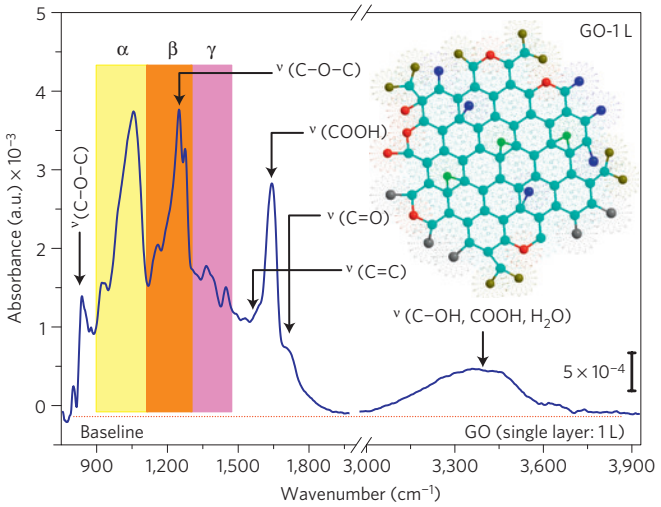

Figure 1 | Transmission infrared-absorbance spectrum of GO-1L. Various oxygen configurations in the structure include the vibration modes of epoxide (C–O–C) (1,230–1,320 cm^{-1}, asymmetric stretching; ~850 cm^{-1}, bending motion), sp^2-hybridized C=C (1,500–1,600 cm^{-1}, in-plane vibrations), carboxyl (COOH) (1,650–1,750 cm^{-1} including C–OH vibrations at 3,530 cm^{-1} and 1,080 cm^{-1}), ketonic species (C=O) (1,600–1,650 cm^{-1}, 1,750–1,850 cm^{-1}) and hydroxyl (namely phenol, C–OH) (3,050–3,800 cm^{-1} and 1,070 cm^{-1}) with all C–OH vibrations from COOH and H_2O. Regions of spectral overlap involving mostly C–O and C=O contributions (850–1,500 cm^{-1}) are broken down into three regions: the α-region (900–1,100 cm^{-1}), β-region (1,100–1,280 cm^{-1}) and γ-region (1,280–1,500 cm^{-1}) (Supplementary Fig. S1). a.u., absorbance units. The red dotted line is the baseline. Inset, Schematic representation of functional groups including epoxide (green), C=C (aqua), C–O (red), C–OH (blue), COOH (brown) and C=O (grey).

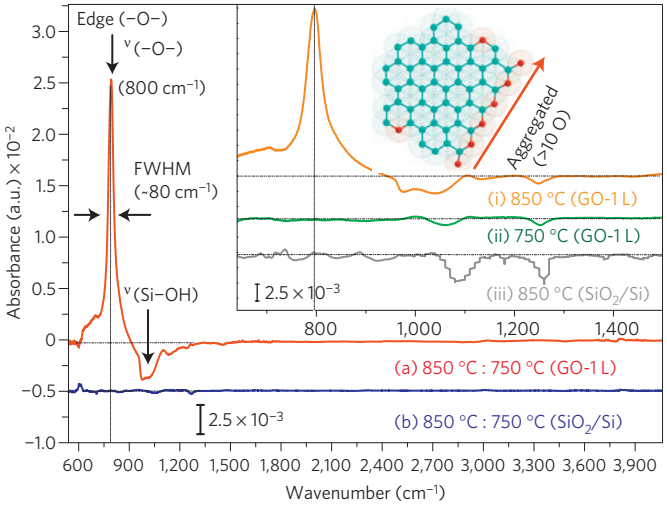

Figure 2 | Transmission infrared absorption spectra of thermally reduced GO-1L after annealing at 850 °C. Differential spectra: ratio of absorbance spectra of 850: 750 °C anneals for GO-1L (a) and SiO_2/Si (b). A new peak appears at 800 cm^{-1} with a full-width at half-maximum of ~80 cm^{-1}. A negative contribution at ~980 cm^{-1} corresponds to the loss of Si–OH from the underlying SiO_2 substrate. The inset shows the absorbance spectra for GO-1L after 850 °C (i) and 750 °C (ii) anneals and for a bare clean SiO_2/Si surface at 850 °C referenced to the room-temperature clean SiO_2/Si surface (iii). The dashed–dotted lines are baselines. In the schematic representation, the remaining aggregated cyclic edge ether (–O–) is presented in red.

observed in each spectral range on reduction can then be used to estimate the concentration of various oxygen species, assuming similar dipole moments (approximately valid within a factor of ~2; ref. 24).

There is a dramatic change after annealing GO samples above 750 °C. Figure 2 presents both the differential and absorbance spectra for GO-1L after 750 °C and 850 °C anneals. After 850 °C anneal, a strong absorption feature appears at 800 cm^{-1} with negligible changes in the rest of the infrared spectra. The spectral loss at ~980 cm^{-1} is not related to GO, but arises from the removal of hydroxyl (Si–OH) on the SiO_2 substrate at 850 °C (refs 25,26). Similar results are obtained in three layers of GO (Supplementary Fig. S2).

The origin of the 800 cm^{-1} mode is unravelled by first-principles calculations. The results of an exhaustive search reveal that the most energetically stable structure with a normal mode in the 800 cm^{-1} region is an aggregated edge-oxidized structure with a row of adjacent ether configuration. For this specific structure, using a structural model shown in Fig. 3a, all vibrational frequencies involving the oxygen motions are calculated. Within the energy range of interest, there are six modes that involve significant O displacements, labelled '1', '2' and so on. Mode 4 departs from other modes in that it involves a displacement of oxygen perpendicular to the edge. The observed infrared peak at 800 cm^{-1} can be assigned to Mode 4 in Fig. 3 (calculated at 870 cm^{-1}), using the correction factor of −55 cm^{-1} and considering error bars (see Theoretical Method). This frequency is not very sensitive to the width of the model nanoribbon used (<10 cm^{-1} variation for twice the width), indicating that it is not a result of the nanoribbon geometry but just the edge geometry. The frequency of this configuration increases as the number of adjacent oxygen atoms decreases (more finite system) as shown in Supplementary Fig. S4, suggesting that the experimental system is composed of at least ten edge oxygen atoms in a row. Such an agglomeration is supported by the fact that agglomerated edge ether groups have the highest binding energy, twice that of non-aggregated ether species and higher than other oxygen configurations (Table 1). It is therefore expected to be the only remaining form of oxygen after annealing to temperatures as high as 850 °C.

The intensity of the 800 cm^{-1} mode is unexpectedly high in comparison to all the other normal modes of the same structure and to the overall intensity of all existing oxygen species measured at 750 °C. Figure 4 summarizes the total intensity of all the oxide modes of GO-1L as a function of thermal annealing. The initial integrated intensity decreases from 0.4 cm^{-1} to ~0.01 cm^{-1} after 750 °C anneal, when only 5–7 at.% of oxygen remains. Note that the coverage of oxygen is related to the intensity although not completely linear, because the dipole moment of each species varies (for example, the dipole moment of carboxyl is the strongest and that of ether the weakest), with a difference of ~2 based on many parameters, most importantly polarity of individual molecules[24]. On annealing to 850 °C, the total integrated area of the asymmetric stretch mode of the edge oxygen (mode centred at 800 cm^{-1}) is ~1.0 cm^{-1}, namely a factor of ~100 higher than the sum of all oxide modes observed after 750 °C anneal. As the oxygen concentration is expected to be similar to or lower than that after 750 °C anneal, this observation indicates that a large enhancement process must be taking place (similarly ~40 times enhancement is observed in GO with three layers; see Supplementary Fig. S5). This selective and large enhancement of the mode at 800 cm^{-1} suggests that it cannot have only a vibrational origin, unless some chemistry takes place between the SiO_2 substrate and the reduced GO.

To test this unlikely possibility, experiments were carried out using different GO thicknesses (one, three and multiple layers) by thermal reduction. All GO layers showed a similar effect on thermal annealing, with the intensity of the 800 cm^{-1} mode depending

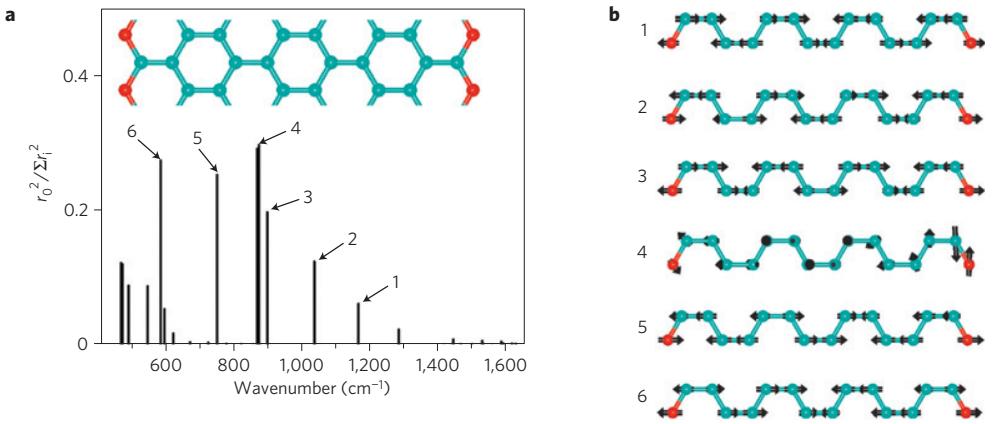

Figure 3 | Simulated vibration modes of edge-oxidized graphene nanoribbon. a, Normal-mode frequencies and magnitudes of the associated oxygen displacements. The structural model represents aggregated edge ether with 14 C and two O atoms in the unit cell. Only six modes with significant O displacement are selected and numbered in order of decreasing frequency. **b**, The shape of atomic motions for each of these six modes, with an arrow length proportional to the magnitude of displacement.

Table 1 | Corresponding binding energies for various oxygen functionalities calculated from *ab initio* simulations.

Chemical species	Binding energy (eV/functionality)
Hydroxyl (C–OH)	1.5 eV/OH
Epoxide (C–O–C)	3.1 eV/O
Carboxyl (COOH)	5.8 eV/COOH
Ketonic species (C=O)	8.0 eV/O
Ether species (C–O) (non-aggregated)	4.9 eV/O
Aggregated cyclic edge ether (–O–)	9.1 eV/O

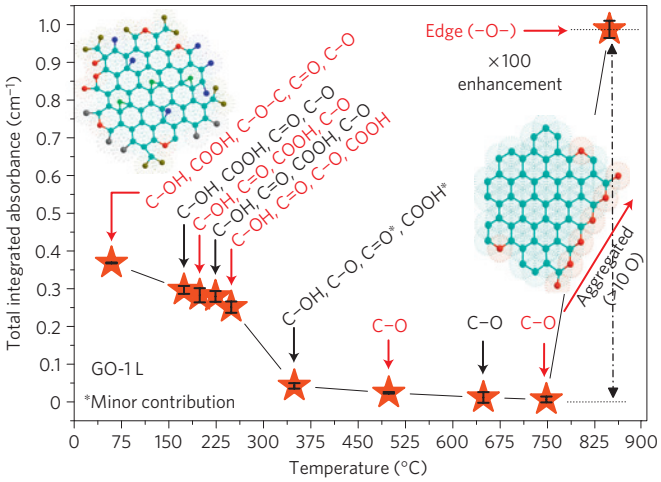

Figure 4 | Total integrated absorbance versus annealing temperatures measured at 60 °C for GO-1L. The existing functional groups at each specific temperature are listed in order of intensity (related to concentration). Almost all of the functional groups disappear at 350 °C and only the C–O containing cyclic-edge-ether contribution remains thereafter. The peak at 800 cm^{-1} shows an intensity enhancement of ~100 times compared with that of all remaining modes at 750 °C. The s.d. values (0.1–2%) shown with error bars are obtained from the mean values of fluctuations in the values of total integrated areas (Supplementary Method). The total integrated absorbance unit is abbreviated as 'cm^{-1}'. The asterisks indicate very small contributions from both carbonyl and carboxyl species.

on how well all forms of oxides other than the aggregated edge oxygen are removed. To check that the substrate did not play a role in reoxidizing the partially reduced GO, multilayer GO samples were reduced chemically (in hydrazine monohydrate) in a closed round-bottom glass flask with a mounted reflux condenser running in an oil bath preheated at 100 °C as described in ref. 27. Each sample was removed at different times of reaction and rinsed in methanol to terminate the reaction and then in distilled water before infrared examination (see the Methods section for details). Once most of the oxide species (especially out-of-plane or terminal oxides, such as hydroxyl, epoxide, carboxyl and ketonic-type species, Supplementary Fig. S6a) are removed, a mode appears at 800 cm^{-1} with an enhanced infrared-absorption intensity (Supplementary Fig. S6b). After extensive immersion in hydrazine monohydrate (two days), all oxygen atoms are removed and the 800 cm^{-1} mode disappears, which strongly supports its assignment.

These and complementary test experiments (Supplementary Section S2) confirm that this strong mode is not due to reoxidation or contamination of the graphene (or SiO_2 substrate), but is an intrinsic phenomenon of the presence of cyclic edge ether adjacent to graphene domains (albeit defective). The participation of electrons is therefore suspected, and first-principles calculations are carried out to better understand the dramatic enhancement of this specific edge-ether normal mode (that is, asymmetric C–O–C stretch) and the absence of enhancement of the other normal modes.

The electronic structures of the six normal modes associated with edge ether are described in Supplementary Fig. S7. All modes involve an oxygen motion perpendicular to the C–O–C axis and are extended throughout the lattice, except Mode 4, which involves an oxygen displacement along this axis and is localized at the edge. The red curves show the positions of the energy bands under the normal-mode deformations (that is, with the oxygen displaced from its equilibrium position) for the six modes correspondingly. All six modes show electronic-structure changes under such normal-mode deformations, but only Mode 4 has an unusual electronic-structure change at the Γ-point, as shown in more detail in Fig. 5a,b. In these panels, the oxygen σ band is indicated in red. At its equilibrium position (that is, before Normal Mode 4 is activated), the undeformed state (Fig. 5a) has an oxygen σ-band located ~1 eV above the Fermi level at the Γ-point. As the atomic configuration deforms according to the displacement of Normal Mode 4 (Fig. 5b), the oxygen σ-band is lowered below the Fermi level and occupied by electrons transferred from the oxygen π-band and carbon π-bands.

Figure 5c shows the electronic-density changes between the deformed (Fig. 5b) and undeformed (Fig. 5a) configurations. The

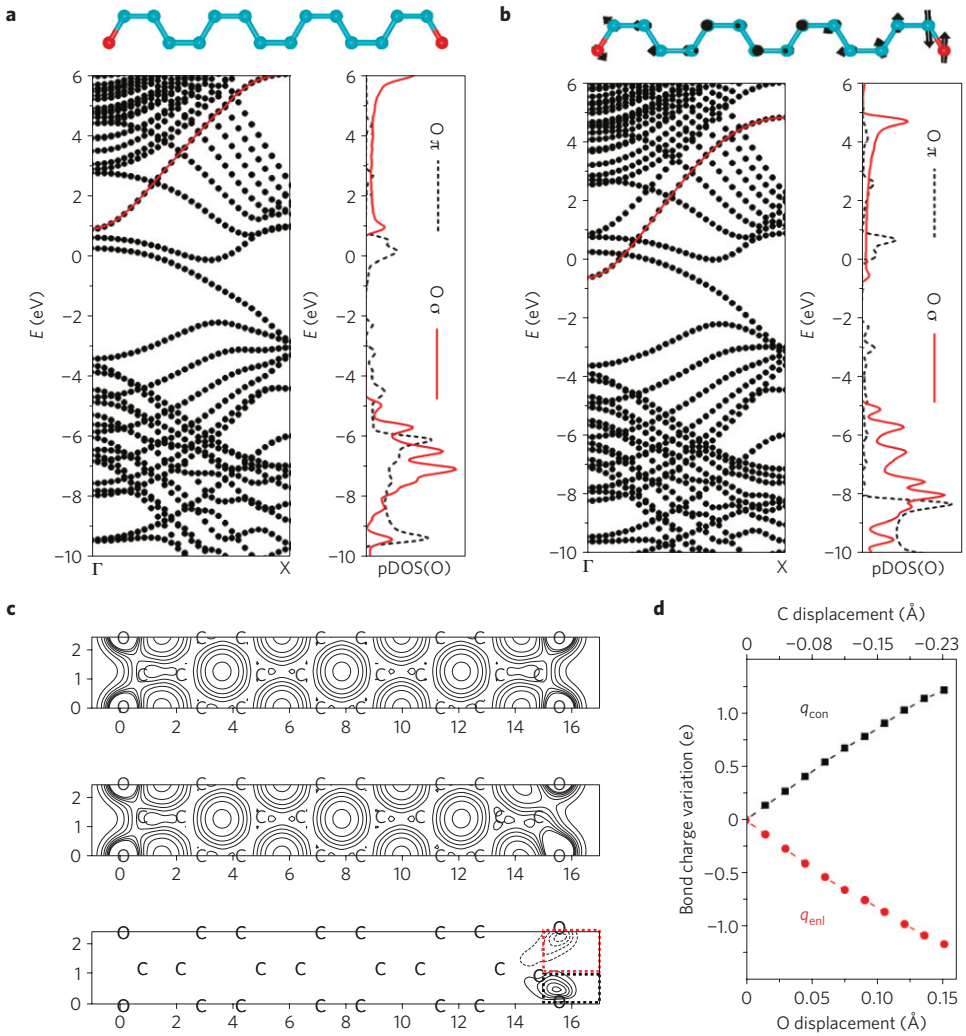

Figure 5 | Electronic-structure change under asymmetric C–O–C stretch-mode vibration of edge-oxidized graphene nanoribbon. a, Ground-state configuration and associated band structure with density of states projected onto the O π- and O σ-orbitals. **b**, The same information for the excited configuration. **c**, Contour plot of two-dimensional electron densities after summation over the plane-normal direction for the ground (top) and excited (middle) configurations. Only one unit cell is shown along the ribbon axis, where lateral atomic positions are indicated in units of angstroms. The bottom panel shows the electron-density increase (solid) or decrease (dashed) after normal-mode displacement. The contour lines map the magnitudes of 0.4, 0.8, 1.2, 1.6, 2.0 e Å^{-2} with proper signs for the bottom panel. **d**, Variation of the total number of electrons inside the red (q_{enl}) or black (q_{con}) rectangular sections in **c** with respect to ground-state value as a function of edge C or O displacement along the ribbon axis.

electronic-charge distribution is clearly localized at the edge C–O–C structures, on one side of the oxygen atom. Figure 5d shows that there is an electronic-charge transfer between the asymmetric C–O bonds as a function of the Mode-4 deformation: the shorter C–O bond (black box in Fig. 5c) gains substantial electron density from the longer C–O bond (red box in Fig. 5c), as quantified by the corresponding black and red curves in Fig. 5d. Furthermore, there is a strong dispersion of the occupied oxygen σ-band, indicating that there are mobile electron states (metallic character) localized at the edge. The appearance of free electrons (that is, a density of electronic states at the Fermi level in the oxygen-induced electronic band in Fig. 5b) localized in the immediate vicinity of the oxygen atom (see Fig. 5c) is therefore correlated to the motion of the edge C–O–C atoms during the excitation of Normal Mode 4.

The presence of these free electrons opens a new absorption channel. There are thus two components of the dynamic dipole moment, $\mu = \mu^{i} + \mu^{e}$, where $\mu^{i} = e_i^*/(2\,M_i^*\omega_0)^{1/2}$ is the ionic contribution and $\mu^{e} = e_e^*/(2m_e^*\omega_0)^{1/2}$ is the electronic contribution[28–30]. The corresponding effective charges are $e_i^* \sim 0.2$–$0.4\,e$ and $e_e^* \sim 0.6\,e$ (from Fig. 5d), where e_i^* is the ionic charge and e_e^* is the electron charge (density). The calculated effective atomic masses are $M_i^* \sim 21\,m_p$ (effective atomic mass) and $m_e^* \sim 0.24\,m_e$ (effective electron mass), where $m_p = 1.67 \times 10^{-24}$ g and $m_e = 9.11 \times 10^{-28}$ g. Clearly, the electronic dipole moment is much larger than the ionic dipole moment for $\omega_0 = 2\pi c\upsilon_0$ (for $\upsilon_0 = 800\,\mathrm{cm}^{-1}$) mostly because of the low mass of the electron. The approximate infrared-absorption enhancement resulting from the presence of free electrons is $|\mu^{e}/\mu^{i}|^2 = (e_e^*/e_i^*)^2 \times (M_i^*/m_e^*) \sim 10^5$. Therefore, the metallic nature of the edge-localized oxygen σ-band is critical for producing the large enhancement of the infrared absorption.

The fact that the experimentally measured enhancement is substantially smaller (~40–100) suggests that only ~0.04–0.1% of the remaining oxygen atoms (out of the ~5–7 at.% present after thermal reduction) are agglomerated with at least ten adjacent atoms. This observation is consistent with the fact that the reduced GO is highly defective and oxygen rearrangement to form straight rows of edge oxygen on annealing is difficult.

This phenomenon resembles the Fano process, because it involves electronic absorption[31], but is in fact fundamentally different. Whereas the Fano absorption consists of a modulation of

an existing electronic (broadband) absorption, this process involves the induction of a metallic density of states at the edge, which is constrained to be in phase with Mode-4 oscillation, so there is no phase difference. Consequently, the resulting infrared-absorption band is symmetric, in contrast to Fano line shapes. Furthermore, there is a genuine enhancement in infrared absorption due to a new absorption channel, instead of a modulation of an existing broadband (electronic) infrared absorption.

Interestingly, the number of adjacent oxygen atoms is critical to both the enhancement and frequency of Mode 4. Indeed, Supplementary Fig. S4 shows that finite edge-ether configurations (that is, with only two, three, four, five and seven adjacent oxygen atoms) exhibit Mode-4 frequencies higher than 900 cm^{-1} (Supplementary Fig. S4e) and are characterized by edge-localized oxygen σ-states that remain above the Fermi level under the same amount of normal-mode displacement as shown in Fig. 5b. For a seven-adjacent edge-ether system, for instance, the oxygen σ-band becomes occupied only after 0.15 Å of oxygen atomic displacement (corresponding to a total system-energy increase of 0.9 eV per O atom) compared with 0.04–0.06 Å of oxygen atomic displacement (corresponding to a total energy of 0.13–0.22 eV/O) for the larger ether-group configuration shown in Fig. 5.

The phonon energy of Mode 4 is $\hbar\omega = 0.11$ eV and the potential energy of one phonon mode is $\hbar\omega(1 + 1/2) = 0.17$ eV. The comparison of the phonon energy and the potential energy of Normal Mode 4 shows that one phonon excitation by infrared absorption induces a large enough deformation to bring the metallic state to the Fermi level. This result explains why it is critical to form a large number of adjacent edge ether groups to enable the softening of Mode 4 so that the metallic state at the Γ-point can be formed. Once the metallic electronic state is formed, the electronic absorption far exceeds the ionic standard C–O–C absorption, so that the excited electron energy at the edge ether group can further excite Mode 4 through electron–phonon coupling. Such a process increases the number of Mode-4 phonons such that the potential energy of Mode 4 will increase to $\hbar\omega(n + 1/2)$, leading to an increased number of metallic electrons.

The above results show that a large density of edge-localized mobile electrons is generated during the oxygen displacement occurring throughout the Mode-4 vibration, if the number of adjacent oxygen atoms is higher than ∼10, owing to an energy decrease of its low-lying oxygen σ-states. In this mechanism, the presence of an area of bare graphene with metallic properties is necessary for the activation of the edge-localized metallic electronic states. If the graphene basal plane near the edge is functionalized by hydroxyl or epoxide groups, carbon π-bands are saturated, resulting in an open bandgap. Furthermore, the chemical-potential difference of the graphene basal plane and the functional groups shifts the Fermi level of the GO such that the edge ether groups have different electron occupation behaviour under normal-mode deformations.

Altogether, these results fully account for the giant increase of infrared absorbance. During the thermal anneal up to 750 °C, the functional groups on the basal plane are mostly desorbed and rearranged to gradually increase the edge-ether-group size (thermodynamically driven reconfiguration of neighbouring oxygen species into cyclic edge ether). During 850 °C anneal, all functional groups other than the edge ether are removed and the number of adjacent edge oxygen configurations becomes large enough that the edge-localized metallic states can be occupied during the Mode-4 displacement.

The lack of similar oxygen rearrangement at the edges during chemical reduction in hydrazine monohydrate at ∼100 °C results in dramatically lower enhancement of the 800 cm^{-1} mode, which is only observed owing to an initial arrangement of adjacent edge ether groups. These findings suggest that cyclic edge ether is formed initially during the GO synthesis, which is in the form of C–O containing species such as lactol[32], peroxide, dioxolane and so on along with other oxide groups (epoxide, hydroxyl, ketone and so on).

The combination of *in situ* infrared-absorption measurements and first-principles calculations reveals that a new oxygen configuration, a set of adjacent edge ether groups, is formed on GO synthesis and further developed on thermal annealing to ∼850 °C. This cyclic edge ether is characterized by a giant infrared absorption when there are more than ∼10 adjacent oxygen atoms and all other forms of oxygen moieties (such as epoxide, hydroxyl, carboxyl and carbonyl) are removed. This giant absorption is due to the in-phase electron band population with mobile electrons localized at the edge and resulting in strong electronic absorption (∼10^5 enhancement). This phenomenon is distinct from non-adiabatic absorption mechanisms (for example, Fano processes), in which the absorption is originating from the electrons, and is then modulated by the phonon motion. In this case, the electronic absorption is induced by the displacement of the oxygen atoms and therefore in phase with the phonon mode (that is, there is no derivative lineshape as is the case for the Fano process). The enhancement is due instead to a new absorption channel, characterized by remarkably narrow induced electron absorption.

This work suggests that the strong 800 cm^{-1} signature of edge oxygen should be observed in carbon nanotubes that have been unzipped by chemical oxidation[33] if they are subsequently annealed to ∼850 °C. Similar effects may also be observed for chemical termination other than oxygen (for example nitrogen, sulphur). Thus, this new phenomenon opens the door to tailoring giant infrared absorption at different spectral positions by modifying the nature of the edge termination. Such control would impact a number of applications such as bandpass filters, resonant detectors, thermal-infrared remote sensing (night vision) and as a solar absorber for energy harvesting.

Methods

Experimental methods. All single-, three- and multilayer GO samples were synthesized using Hummer's[34] method. Single- and three-layer GO samples were transferred by a vacuum-filtration technique described in refs 15,23 on bare clean surfaces of SiO_2/Si (Supplementary S3) and then characterized using atomic force microscopy and Raman spectroscopy as indicated in refs 15,35. Multilayer GO samples were purified using the method in ref. 36 and 2% (wt/vol.) of prepared aqueous solution was deposited on the surface by drop casting.

The annealing chamber (a closed system) is placed in the main compartment of a N_2-purged spectrometer (Thermo Scientific Nicolet 6700 FT–IR spectrometer with a KBr beam splitter, a deuterated triglycine sulphate detector and constant nitrogen flow generated by a slight overpressure). The sample in the chamber is positioned so that the infrared incident angle is close to the Brewster angle (70°) using direct transmission. The chamber is evacuated (10^{-3}–10^{-4} torr) to minimize environmental effects. The sample is held by two tantalum clips to permit resistive heating in vacuum (6010A d.c. power supply, 0–200 V/0–17 A, 1,000 W, Hewlett Packard). Once the sample is in place, the measurements are *in situ* (no sample transfer needed). All temperature readings are monitored by a Eurotherm unit using type-K thermocouples spot-welded to a Ta clip attached to the sample edge. Calibration with a pyrometer indicates that the thermocouple readings are systematically too low (∼20–50 °C) in the 500–900 °C range. However, this is a systematic error, so the relative measurements are reproducible.

For each annealing temperature, the total integrated absorbance in the transmission infrared differential spectra is calculated by summing all oxygen-containing group contributions (subtracting the C=C contribution and SiO_2 peaks when necessary from deconvoluted peak areas). Fittings are performed using Aanalyzer fitting software including both Lorentzian and Gaussian contributions with 20 iterations for maximized R^2 values to minimize the error in the iteration progress, allowing a negative peak-area contribution as well when necessary. Standard deviations (Supplementary Method) are calculated from the mean values of both baseline-corrected data and data with no corrections.

Chemical reduction of GO was performed using 32.1 mmol of hydrazine monohydrate ($N_2H_4 \cdot H_2O$, 64–65%, reagent grade, 98% from Sigma-Aldrich) in distilled water (purified by Millipore, Milli-Q Element A10 equipped with an ultrapure ion-ex cartridge) at 100 °C under refluxing in a three-neck round-bottom flask for two days as described in ref. 27. 1 ml of sample was taken from the solution at different reaction times during refluxing using a syringe with a stainless-steel

needle without stopping the reaction or changing any condition in the closed system, and the reaction was terminated with methanol by transferring in a glass vial. Each sample was purified by washing with distilled water several times to remove the residuals and this was repeated for each time-dependent study of the GO reduction process. Each sample in aqueous solution was then transferred onto a clean Si/SiO_2 substrate, dried in vacuum and taken immediately into the main compartment under constant nitrogen purge for further transmission infrared measurements (<1 min in air).

Theoretical methods. To calculate infrared intensities, we solve within a harmonic approximation the following eigenvalue equation (1):

$$\sum_{j\beta} D_{i\alpha,j\beta} u_{j\beta} = \omega^2 u_{i\alpha} \quad (1)$$

to obtain normal-mode frequency ω and eigenvector $u_{i\alpha}$, where i and j are atomic indices and α and β label the Cartesian coordinates. The dynamical matrix $D_{i\alpha,j\beta}$ is obtained by the second derivative of the total energy with respect to atomic displacements $R_{i\alpha}$ and $R_{j\beta}$, that is $D_{i\alpha,j\beta} = \partial^2 E/\partial R_{i\alpha}\partial R_{j\beta}$. Once the normal-mode ${u_{i\alpha}}^k$ is known for the kth mode, its absolute infrared intensity I^k can be written as

$$I^k = \left| \frac{\mathrm{d}\mu^k}{\mathrm{d}q} \right|^2 \quad (2)$$

with the normal-mode coordinate q defined as $\mathrm{d}R^k_{i\alpha} = {u_{i\alpha}}^k \mathrm{d}q$. The dynamic electric dipole moment can be expressed as $\mathrm{d}\mu^k_\alpha = \Sigma_i Z^*_i \mathrm{d}R^k_{i\alpha}$, where Z^*_i denotes the effective charge of the ith atom. From these two relations, we use a simplified form to compute the intensity:

$$I^k = \left(\sum_i Z^*_i u^k_{ix}\right)^2 + \left(\sum_i Z^*_i u^k_{iy}\right)^2 + \left(\sum_i Z^*_i u^k_{iz}\right)^2 \quad (3)$$

The total energy is computed using a Vienna *ab initio* simulation package[37] with projector augmented wave pseudopotentials[38] for the electron–ion interaction and the local-density approximation[39] for the exchange–correlation functional. The energy cutoff of 500 eV is used for the plane-wave basis expansion. The effective charge is obtained from Bader charge analysis[40]. We use a finite-size cluster representing a specific oxidation group with the edge C dangling bonds passivated by H atoms and with the 10 Å vacuum region to decouple the interaction between periodic images. The uncertainty associated with the calculated vibrational frequency is less than 10 cm^{-1}, and the effective charge less than 0.2 e, which leads to small errors in overall infrared peak position and intensity. However, our simulation predicts larger frequencies than the experimental values by 55 cm^{-1}, as verified by calculating the stretching mode of a gas CO (2,225 cm^{-1} from our method, in comparison with the experimental value of 2,170 cm^{-1}; ref. 41). The main source of such discrepancy is the local-density approximation.

Received 18 January 2010; accepted 18 August 2010; published online 19 September 2010

References

1. Kharissova, O. V. & Kharisov, B. I. Graphenes, one of the hottest areas in the nanotechnology: attention of chemists is needed. *Open Inorg. Chem. J.* **2,** 39–49 (2008).
2. Novoselov, K. S. *et al.* Electric field effect in atomically thin carbon films. *Science* **306,** 666–669 (2004).
3. Wallace, P. R. The band theory of graphite. *Phys. Rev.* **71,** 622–634 (1947).
4. Novoselov, K. S. *et al.* Two-dimensional gas of massless Dirac fermions in graphene. *Nature* **438,** 197–200 (2005).
5. Berger, C. *et al.* Electronic confinement and coherence in patterned epitaxial graphene. *Science* **312,** 1191–1196 (2006).
6. Morozov, S. V. *et al.* Giant intrinsic carrier mobilities in graphene and its bilayer. *Phys. Rev. Lett.* **100,** 016602–016606 (2008).
7. Wu, J. *et al.* Organic solar cells with solution-processed graphene transparent electrodes. *Appl. Phys. Lett.* **92,** 263302–263304 (2008).
8. Geim, A. K. & Novoselov, K. S. The rise of graphene. *Nature Mater.* **6,** 183–191 (2007).
9. Khveshchenko, D. V. Coulomb-interacting Dirac fermions in disordered graphene. *Phys. Rev. B* **74,** 161402–161406 (2006).
10. Morozov, S. V. Strong suppression of weak localization in graphene. *Phys. Rev. Lett.* **97,** 016801–016804 (2006).
11. Pisana, S. *et al.* Breakdown of the adiabatic Born–Oppenheimer approximation in graphene. *Nature Mater.* **6,** 198–201 (2007).
12. Cai, W. *et al.* Synthesis and solid-state NMR structural characterization of ^{13}C-labelled graphite oxide. *Science* **321,** 1815–1817 (2008).
13. Park, S. *et al.* Graphene oxide papers modified by divalent ions enhancing mechanical properties via chemical crosslinking. *ACS Nano* **2,** 572–578 (2008).
14. Eda, G., Mattevi, C., Yamaguchi, H., Kim, H. & Chhowalla, M. Insulator to semimetal transition in graphene oxide. *J. Phys. Chem. C* **113,** 15768–15771 (2009).
15. Mattevi, C. *et al.* Evolution of electrical, chemical and structural properties of transparent and conducting chemically derived graphene thin films. *Adv. Funct. Mater.* **19,** 2577–2583 (2009).
16. Ferrari, A. C. Raman spectroscopy of graphene and graphite: Disorder, electron–phonon coupling, doping and nonadiabatic effects. *Solid State Commun.* **143,** 47–57 (2007).
17. Bruna, M. & Borini, S. Assessment of graphene quality by quantitative optical contrast analysis. *J. Phys. D* **42,** 175307–175311 (2009).
18. Garcia-Sanchez, D. *et al.* Imaging mechanical vibrations in suspended graphene sheets. *Nano Lett.* **8,** 1399–1403 (2008).
19. Lo, C. P., Quattrochi, D. A. & Luvall, J. C. Application of high-resolution thermal infrared remote sensing and GIS to assess the urban heat island effect. *Int. J. Remote Sens.* **18,** 287–304 (1997).
20. Dresselhaus, M. S. Nanotube antennas. *Nature* **432,** 959–960 (2004).
21. Parasido, J. A. & Starner, T. Energy scavenging for mobile and wireless electronics. *IEEE Pervasive Comput.* **4,** 18–27 (2005).
22. Xia, F. *et al.* Ultrafast graphene photodetector. *Nature Nanotech.* **4,** 839–843 (2009).
23. Goki, E., Giovanni, F. & Chhowalla, M. Large-area ultrathin films of reduced graphene oxide as a transparent and flexible electronic material. *Nature Nanotech.* **3,** 270–274 (2008).
24. Lide, D. R. *CRC Handbook of Chemistry and Physics* 84th edn (CRC Press LLC, 2003).
25. Hartwig, C. M. & Rahn, L. A. Bound hydroxyl in vitreous silica. *J. Chem. Phys.* **67,** 4260–4261 (1977).
26. Fukui, K., Miyauchi, H. & Iwasawa, Y. Highly sensitive detection of adsorbed species on a SiO_2 surface by reflection absorption infrared spectroscopy. *Chem. Phys. Lett.* **274,** 133–139 (1997).
27. Stankovich, S. *et al.* Synthesis of graphene-based nanosheets via chemical reduction of exfoliated graphite oxide. *Carbon* **45,** 1558–1565 (2007).
28. Chabal, Y. J. Surface infrared spectroscopy. *Surf. Sci. Rep.* **8,** 211–357 (1988).
29. Chabal, Y. J. Electronic damping of hydrogen vibration on the W(100) surface. *Phys. Rev. Lett.* **55,** 845–848 (1985).
30. Zhang, Z. Y. & Langreth, D. C. Electronic damping of adsorbate fundamental and overtone vibrations at metal surfaces. *Phys. Rev. B* **39,** 10028–10046 (1989).
31. Tang, T. *et al.* A tunable phonon–exciton Fano system in bilayer graphene. *Nature Nanotech.* **5,** 32–36 (2010).
32. Gao, W., Alemany, L. B., Ci, L. & Ajayan, P. M. New insights into the structure and reduction of graphite oxide. *Nature Chem.* **1,** 403–408 (2009).
33. Kosynkin, D. V. *et al.* Longitudinal unzipping of carbon nanotubes to form graphene nanoribbons. *Nature* **458,** 872–876 (2009).
34. Hirata, M., Gotou, T., Horiuchi, S., Fujiwara, M. & Ohba, M. Thin-film particles of graphite oxide: High-yield synthesis and flexibility of the particles. *Carbon* **42,** 2929–2937 (2004).
35. Mkhoyan, K. A. *et al.* Atomic and electronic structure of graphene oxide. *Nano Lett.* **9,** 1058–1063 (2009).
36. Gilje, S., Han, S., Wang, M., Wang, K. L. & Kaner, R. B. A chemical route to graphene for device applications. *Nano Lett.* **7,** 3394–3398 (2007).
37. Kresse, G. & Fürthmuller, J. Efficient iterative schemes for *ab initio* total-energy calculations using a plane-wave basis set. *Phys. Rev. B* **54,** 11169–11186 (1996).
38. Kresse, G. & Joubert, D. From ultrasoft pseudopotentials to the projector augmented-wave method. *Phys. Rev. B* **59,** 1758–1775 (1999).
39. Ceperley, D. M. & Alder, B. J. Ground state of the electron gas by a stochastic method. *Phys. Rev. Lett.* **45,** 566–569 (1980).
40. Bader, R. *Atoms in Molecules: A Quantum Theory* (Oxford Univ. Press, 1990).
41. Huber, K. P. & Herzberg, G. *Molecular Spectra and Molecular Structure, Constants of Diatomic Molecules* Vol. 4 (Van Nostrand Reinhold, 1979).

Acknowledgements

The authors acknowledge the financial support of the SWAN-NRI program and Texas Instruments (TI), the technical expertise of J-F. Veyan and in-depth discussions with L. Colombo (TI) and with R. M. Wallace, E. Vogel, J. Kim, M. Kim, J-F. Veyan and W. Kirk at UT Dallas.

Author contributions

M.A. carried out all infrared-spectroscopy work, including thermal-annealing experiments in parallel to chemical reduction. G.L. carried out all density functional theory and molecular dynamics simulations using theoretical methods. Y.J.C. and K.C. directed and supervised the experimental and theoretical research, respectively. M.A., G.L., K.C. and Y.J.C. contributed equally to the manuscript. C.M. prepared the single-layer and three-layer graphene oxide samples under M.C.'s supervision.

Additional information

The authors declare no competing financial interests. Supplementary information accompanies this paper on www.nature.com/naturematerials. Reprints and permissions information is available online at http://npg.nature.com/reprintsandpermissions. Correspondence and requests for materials should be addressed to Y.J.C.